Simultaneous Analysis of Ion and Electron Heat Transport by Power Modulation in JET

F. Ryter[1], C. Angioni[1], C. Giroud[2], A.G. Peeters[3], T. Biewer[4], R. Bilato[1], J. Candy[5], E. Joffrin [6], T. Johnson[7], H. Leggate[2], E. Lerche[8], G. Madison[2], P. Mantica[9], D. Van Eester[8], I. Voitsekhovitch[2], R.E. Waltz[5] and JET Contributors *

JET-EFDA, Culham Science Centre, OX14 3DB, Abingdon, UK

[1] *Max-Planck-Institut für Plasmaphysik, EURATOM Association, D-85748 Garching*

[2]*Culham Science Centre, EURATOM/UKAEA Association, OX14 3DB, Abingdon,UK*

[3]*Centre for Fusion Space and Astrophysics, University of Warwick, Coventry 7AL, UK*

[4]*Fusion Energy Division, Oak Ridge National Lab., P.O. Box 2008 MS 6169 Oak Ridge, USA*

[5]*General Atomics, San Diego, CA 92186, USA*

[6]*JET-EFDA-CSU, Culham Science Centre, OX14 3DB, Abingdon, UK*

[7]*EURATOM-VR Association, Fusion Plasma Physic, EES, KTH 10044 Stockholm, Sweden*

[8]*LPP-ERM/KMS, Association Euratom-Belgian State, TEC, B-1000 Brussels, Belgium*

[9]*Istituto di Fisica del Plasma, EURATOM/ENEA-CNR Association, 20125, Milano, Italy*

e-mail contact of main author: ryter@ipp.mpg.de

Abstract

In fusion plasmas, turbulence-driven heat transport generally dominates both electrons and ions channels. It increases above a threshold in normalized gradient with a rate named stiffness. Heating power modulation experiments provide a direct measurement of the stiffness, as already demonstrated for the electrons, but not for ions so far. In this paper, we report, for the first time, results yielding the ion stiffness deduced from modulation experiments. The experiments were carried out in JET plasmas using Ion Cyclotron Resonance Heating in the ^{3}He scheme. The ion stiffness is larger than that of electrons, but remains moderate and is in agreement with the values yielded by non-linear gyro-kinetic calculations. As a fraction of the electron heating is also modulated in these experiments, a comprehensive analysis of both ion and electron heat transport can be carried out simultaneously, together with an experimental assessment of the ICRH heat sources of the ^{3}He scheme.

1 Introduction

In fusion plasmas, turbulent phenomena driven by the Ion Temperature Gradient and Trapped Electron Mode instabilities in general dominate ion and electron heat transport, respectively. The ITG and TEM modes are unstable above respective thresholds in normalized temperature gradients, $R\nabla T/T = R/L_T$, leading to an increase of transport above the threshold. The rate with which transport increases above the threshold is called "stiffness", characterized by a factor χ_s which will be defined below. The observed resilience of the temperature profile shape to changes in heating power deposition, see e.g. [1, 2, 3, 4, 5, 6, 7, 8], can be explained by these properties [9]. For the electrons, the existence of both threshold and stiffness have been directly evidenced experimentally in several devices [10, 11, 12, 13], but only very recently for ions [14]. "Perturbative" transport experiments, in which the temperature perturbation induced by modulating the heating power is analyzed, yields the stiffness properties. Indeed, the propagation of the excited heat pulses is determined by the slope of the heat flux with respect to the temperature gradient, yielding the heat pulse diffusivity [15, 16]:

$$\chi_j^{HP} = -\frac{\partial q_j}{\partial n_j \nabla T_j} = \chi_j^{PB} + \frac{\partial \chi_j}{\partial \nabla T_j}\nabla T_j \qquad (1)$$

where the subscript j denotes e or i (electron or ion), q heat flux and n density, whereas χ_j^{PB} is the usual heat diffusivity from power balance. In the experiments, χ_j^{HP} is derived from the Fourier transform of the

* see appendix of F. Romanelli et al. , this conference paper OV/1-2

temperature data, interpreted in slab geometry [16]. This yields 2 estimates for the heat pulse diffusivity, $\chi_j^{Amp} \propto (\partial \mathrm{Ln}(Amp)/\partial r)^{-2}$ derived from the amplitude profile and $\chi_j^{phi} \propto (\partial \phi/\partial r)^{-2}$ from the phase profile. Due to damping processes, which affect amplitude and phase profiles, these 2 quantities differ at low modulation frequencies ($\chi_j^{phi} \geq \chi_j^{Amp}$), but converge asymptotically towards χ_j^{HP} at high modulation frequencies for which damping becomes negligible. However, in the geometric mean, $\sqrt{\chi_j^{Amp}\chi_j^{phi}}$, the damping effects mathematically cancel and, at any frequency, this quantity can be considered as a good experimental estimator of the actual value of χ_j^{HP}.
The modulation method has been extensively used to investigate electron heat transport properties, [17, 9, 18], but not applied to the ions so far. The main goal of the work presented here was to modulate the ion temperature and deduce experimentally, for the first time, the stiffness of ion transport. As a fraction of the electron heating power was also modulated, these experiments allow a comprehensive and simultaneous investigation of both ion and electron heat transport by perturbative methods.

2 Experiments

2.1 Experimental conditions

The experiments presented here have been carried out in the JET tokamak, $R \approx 3$m and $a \approx 1$m, at a rather high edge safety factor value, $q_{95} \approx 6$ to avoid sawteeth. They were run in deuterium L-modes at a density of about $3 \times 10^{19}\mathrm{m}^{-3}$, heated by Neutral Beam Injection as background heating and Ion Cyclotron Resonance Heating in the ^{3}He minority scheme for the power modulation part. The RF power was modulated at f_{mod} with a 50/50 duty-cycle and a modulation amplitude of about 80%. JET offers a unique opportunity for localized ion and electron heating by ICRH in the ^{3}He minority scheme, whose heating properties depend on the ^{3}He concentration [^{3}He]. For [^{3}He] $\approx 8\%$, there is a maximum of ion heating from the ICRH-accelerated ions which deliver a dominant fraction of their energy to the plasma as ion heating, significantly more than in the hydrogen minority scheme. The power deposition is calculated by the time-dependent PION code [19], yielding the ICRF heat sources for analyses and transport simulations. We also get ICRH power deposition profiles from the SELFO code which is not time-dependent but provides a more accurate distribution of the power in the different channels.
The essential measurement of the ion temperature is provided by the CXRS diagnostic. The experiments have been carried in three distinct series of discharges, in 2002, 2003 and 2006. In the 2002 and 2003 campaigns, the time resolution of the T_i measurement was 50 ms which limited the maximum modulation frequency to about 4 Hz. The 2002 discharges demonstrated that it was possible and meaningful to address ion perturbative transport with this scenario. In the 2003 series, we varied the NBI heating to investigate the possible influence of T_i. These 2 series yielded good results, which however required validation by experiments at higher modulation frequencies. This was finally possible in the 2006 campaign for which the CXRS diagnostic had been updated, providing 2 separate measurements (CXFM and CXGM) each with a time resolution of 10ms. We obtained good modulation data from an ICRH modulation frequency scan $4 \leq f_{mod} \leq 20$ Hz. As these discharges were carried out at the very beginning of the experimental campaign, due some unfortunate technical difficulties, the data from the third core CXRS and edge CXSR diagnostics turned out to be incorrect. As shown below, not only the modulation of T_i but also that of T_e are analyzed in these experiments. The T_e measurement is provided by the Electron Cyclotron Emission radiometer diagnostic.

2.2 Analysis of the modulated T_i data

The analysis of the T_e modulation by Fourier transform is a widely used method in transient transport studies. The high time resolution of the ECE diagnostic does not limit the modulation frequency and its high sensitivity provides in general data with a very good signal-to-noise ratio.
The situation for T_i is different: the time resolution of the CXRS data can limit the highest modulation frequency. This was the case for the 2002 and 2003 series with the 50ms time resolution. The 10ms exposure time available for 2006 provided much better conditions and room for optimizing the signal-to-noise ratio. The best S/N is a compromise between the integration time on which the T_i analysis is carried out and the number of measurement points available for the Fourier transform. In our experiments, several CXRS exposure frames with 10ms integration time can be grouped prior to the T_i analysis. At low modulation frequency, up to 5 frames can be grouped without affecting the phase. This demonstrates the validity of the 2002 and 2003 data with 50ms resolution at 4 Hz. With 10 ms exposure time, the

quality of the modulated T_i data is good under our experimental conditions and the best S/N is obtained when grouping at most 2 or 3 frames, depending on the cases. Thus, for 2006, the availability of two independent CXRS systems and the possibility of grouping the frames provides an excellent set of data to investigate the heat pulse propagation in the frequency scan.

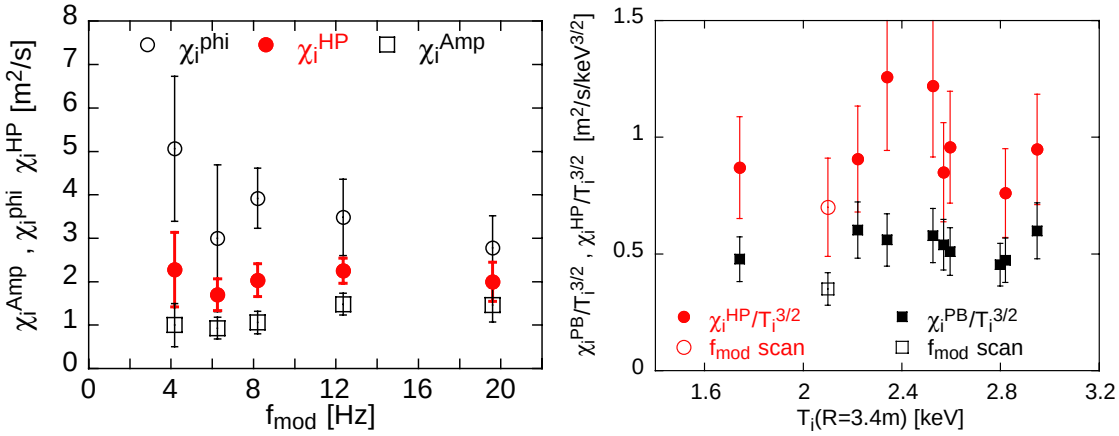

Figure 1: *Experimental results from perturbative transport analyzed at $R = 3.4$ m. Left plot: Frequency dependence of χ_i^{phi}, χ_i^{Amp} and χ_i^{HP} versus f_{mod}. Right plot: normalized values of χ_i^{HP} and χ_i^{PB} versus ion temperature from the NBI power scan, the open symbols are representative of the f_{mod} scan results.*

The perturbative transport results of the frequency scan, represented by χ_i^{phi}, χ_i^{Amp} and χ_i^{HP} versus f_{mod} analyzed at about mid-radius ($R \approx 3.4$ m), are plotted in the left plot of Fig. 1. The values are the mean of all the realistic fits which can be made using the available data for each frequency, whereas the error bars are provided by the corresponding standard deviation. As predicted, χ_i^{phi} is larger than χ_i^{Amp} and these quantities converge towards χ_i^{HP} as f_{mod} increases. The value of χ_i^{HP} is close to $2\mathrm{m}^2/\mathrm{s}$ and does not depend on f_{mod}. This frequency scan indicates, for the first time, that ion perturbative transport behaves as expected. Therefore, we conclude that this method can be used to investigate the properties of ion heat transport. This frequency scan also indicates that the data at $f_{mod} = 4$ Hz, obtained in the 2002 and 2003 series are valid. This is due to the fact that the ion stiffness is not very high, as shown below. Indeed, measuring higher stiffness requires higher modulation frequency to catch the propagation of the heat pulses correctly. In the right plot of Fig. 1, we illustrate the results from the heating power scan of 2002 and 2003 by plotting the normalized transport coefficient $\chi_i^{PB}/T_i^{3/2}$ and $\chi_i^{HP}T_i^{3/2}$ versus T_i. As indicates by the x-axis, the scan provides a significant variation in T_i. Within the error bars, these normalized diffusivities do not vary with heating power, as indicated by the absence of dependence on T_i. As R/L_{T_i} remains constant within 20%, this strongly suggests that the basic characteristics of ion transport do not change significantly in this power scan, also supported by the fact that the ratio χ_i^{HP}/χ_i^{PB} remains constant.

3 Modeling

3.1 The critical gradient model

Turbulence-driven electron and ion heat transport increases above a threshold in R/L_{T_j} with a given stiffness. An empirical model, taking these properties into account, has been developed for electron heat transport and successfully tested on several devices [20, 21, 9]. This Critical Gradient Model (CGM) describes the behaviour of heat diffusivity and is written here in the same form for the electron and ion channels as:

$$\chi_j = \chi_{j,s} q^{3/2} \frac{T_j}{eB} \frac{\rho_j}{R} \left[\frac{R}{L_{T_j}} - \frac{R}{L_{T_{j,crit}}} \right]^{\alpha} H\left(\frac{R}{L_{T_j}} - \frac{R}{L_{T_{j,crit}}} \right) + \chi_{j,0} \qquad (2)$$

where q is the safety factor, B magnetic field and H is the Heaviside step function which mimics the

existence of the threshold. The normalized ion gyro-radius ρ_j is $\rho_s = \sqrt{m_i T_e}/eB$ for the electrons and $\rho_i = \sqrt{m_i T_i}/eB$ for the ions. The stiffness factor is defined as $\chi_{j,s}$ and $R/L_{T_{j,crit}}$ is the threshold. The term $\chi_{j,0}$, which represents transport below the threshold, is in general negligible as soon as R/L_{T_j} is somewhat above the threshold. This is neo-classical transport for the ions and an arbitrary value for the electrons. The gyro-Bohm factor, $T_j/(eB)\rho_j/R \propto T_i^{3/2}$, is commonly used for transport driven by micro-turbulence. Most of the previous studies applying this model for electron transport yielded good results assuming a linear dependence of χ_j versus R/L_{T_j}, i.e. $\alpha = 1$. This implies a quadratic dependence of the heat flux which is not adequate for some cases of the present work, as shown in Sect. 3.3.

3.2 Modulated heat sources by ICRH

In the ICRH ^{3}He minority scheme, the faster RF-accelerated ^{3}He ions deliver their energy by collisions to the electrons, with a long time constant, whereas the slower ones provide ion heating, with a shorter time constant. The respective power densities are $P_{e,coll}$ and $P_{i,coll}$, peaked around the radial position of the ICRF resonance. In addition, direct electron heating by the fast wave occurs, without any time constant, yielding the centrally peaked deposition $P_{e,direct}$. These processes are calculated by the time-dependent PION code, taking into account the RF power modulation. The time-averaged power deposition profiles for a representative shot of the frequency scan are indicated in Fig. 2 left plot. In these discharges, $P_{i,coll}$ and $P_{e,coll}$ are deposited somewhat off-axis, with a maximum at $\rho_{tor} \approx 0.2$, whereas $P_{e,direct}$ is indeed localized on the plasma axis. Due to the time constants of the energy transfer, the modulation amplitudes of $P_{i,coll}$ and $P_{e,coll}$ decrease with f_{mod} whereas the phase delay with respect to the RF power increases, Fig. 2 right plot. Note the large phase delay of $P_{e,coll}$. The points exhibit some scatter which is due to the shot to shot variation of [^{3}He] and collisionality, as tentatively indicated by the error bars. For such discharges, the heating powers yielded by the SELFO code compared to those of PION are: $\approx 0.8 P_{i,coll}$, $\approx 3.2 P_{e,coll}$ and $\approx 0.5 P_{e,direct}$. These differences will be taken into account in the transport simulations.

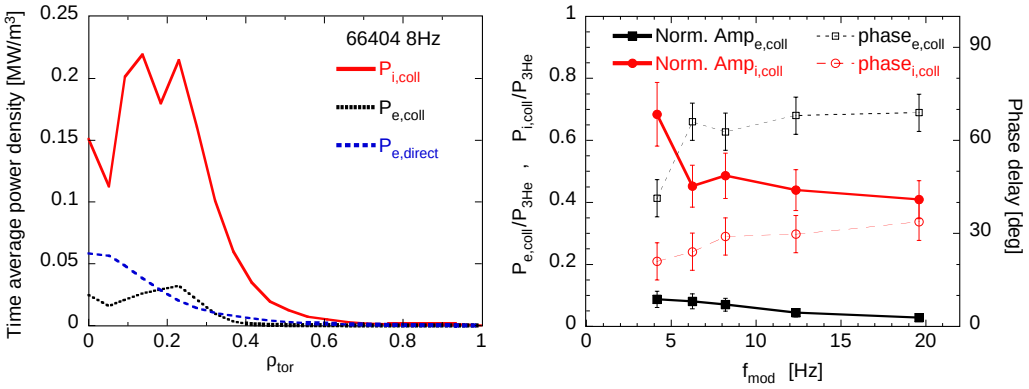

Figure 2: *Results from PION for modulated ICRF. Left plot: profiles of deposited time-averaged power densities. Right plot: Modulation amplitude, normalized to the power absorbed by the minority, and phase delay of the volume-integrated $P_{i,coll}$ and $P_{e,coll}$ versus f_{mod}.*

3.3 Non-linear gyro-kinetic calculations

Based on the experimental data of the 2006 series, non-linear gyro-kinetic calculations, including collisions, have been carried out with the GYRO code, [22]. The calculations are made for the experimental situation at mid-radius. The size of the box was $81\rho_s$ and $113\rho_s$ in the x and y direction respectively, with 180 radial grid points and 32 toroidal modes up to poloidal wave number $k_\theta \rho_s = 1.5$. This toroidal spectrum was found necessary for properly resolved simulations, while simulations with only 16 modes up to $k_\theta \rho_s \approx 1$ were giving significantly different results. We have also verified that simulations with 64 modes up to $k_\theta \rho_s \approx \geq 2$ yield results very similar to the 32 mode cases. We also included the effect of [^{3}He] which contributes through two effects: the dilution of the ion density and the induced change in R/L_{n_i}. In the results shown below we assumed [^{3}He] = 15% with a flat profile which somewhat reduces stiffness and transport with respect to the case with [^{3}He] = 0. We investigated, at constant temperature, the dependence of the heat fluxes q_e and q_i upon R/L_{T_i} and R/L_{T_e} around the experimental values, $R/L_{T_i} = 5$, $R/L_{T_e} = 8.4$ and $R/L_{n_e} = 2$. The experimental values of T_e and T_i are comparable, but the

profile shapes are different yielding the different gradients. The analysis of the GYRO results reveals that heat transport is dominated by the ITG instability in these plasmas with a weak contribution from the TEM. The dependence of q_i and q_e on R/L_{T_i} and R/L_{T_e} are summarized in Fig. 3. The respective contributions from ITG and TEM to the heat fluxes can be deduced from the dependencies of the fluxes on the gradients R/L_{T_i} and R/L_{T_e}, and deduced from the results of Fig. 3. Boxes 1 and 4 correspond the diagonal terms, the usual ion and electron heat conductivities respectively, whereas boxes 2 and 3 represent the off-diagonal contributions. We assume that all four transport channels can be written in the form of the CGM given by Eq. 2 with respective coefficients. In Fig. 3 the points are the single GYRO results and the lines are fits of the form given by Eq. 2 which yield the respective values for χ_s, α and threshold indicated in the boxes. Box 1, ion heat conductivity, shows that the dependence of q_i on R/L_{T_i} is close to linear, as expected for the ITG instability. The ions stiffness is rather low, which is attributed to the situation $R/L_{T_e} > R/L_{T_i}$ and, to a lesser extent, to the presence of ^{3}He. Indeed, setting $R/L_{T_e} = R/L_{T_i}$ almost doubles the stiffness value. Box 2 indicates a strong dependence of q_e on R/L_{T_i} (off-diagonal term) because it represents the ITG contribution to q_e and this reflects that transport is ITG-dominated in these discharges. The other off-diagonal term, illustrated in box 3, represents the contribution of the TEM instability to ion transport. It exhibits almost no dependence of q_i on R/L_{T_e}, this effect is negligible and can be ignored. The value of q_i in this box is due to the ITG instability, driven by R/L_{T_i} as indicated by box 1. Box 4, which corresponds to electron heat conductivity, exhibits a clear dependence of q_e on R/L_{T_e}. As sketched in the figure, the increase of q_e with R/L_{T_e} is to be understood as due to the contribution of the TEM instability to electron heat transport above its threshold $R/L_{T_{e,crit}} \approx 7$, in addition to the dominant ITG part. In this range of R/L_{T_e}, a large part of the electron heat flux is driven by the ITG as indicated by the dependence on R/L_{T_i} shown in box 2. At the nominal experimental value of R/L_{T_e}, the TEM-driven electron heat flux contributes for about 15%.

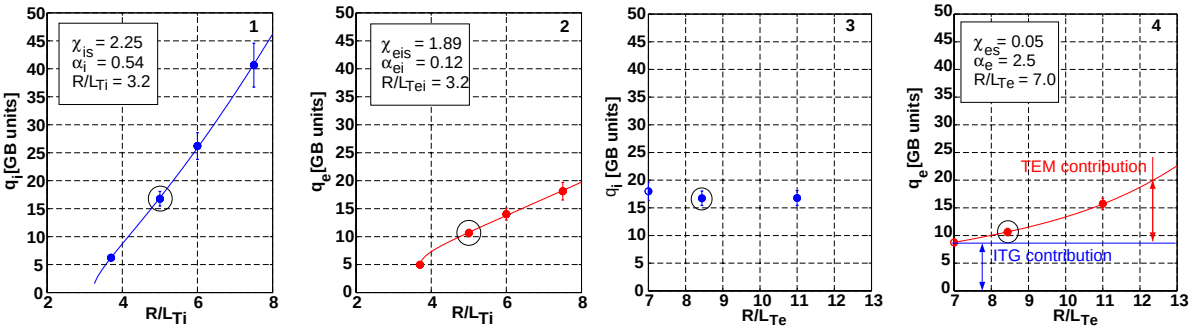

Figure 3: *Results from GYRO: dependence of the heat fluxes on normalized gradients. The encircled points correspond to the nominal experimental values. The coefficients deduced from the fits are indicated in the boxes.*

3.4 Transport modeling

The transport simulations are performed with the ASTRA transport code [23] in which the CGM has been implemented for both ion and electrons. The simulations are time-dependent using the ICRH heat sources provided by the PION code, corrected by the SELFO information, as specified below. The NBI heating profiles are taken from TRANSP, [24]. The calculated time-dependent T_i and T_e are Fourier-analyzed as those from experiments.

We first compared experiment and simulations for T_i, illustrated in Fig. 4 which shows time-averaged T_i profiles, as well as amplitudes and phases of the modulation for discharges at f_{mod} 8 and 20 Hz. The simulations have been carried out with 3 values of $\chi_{i,s}$ around the value yielded by GYRO. The best agreement is achieved with a values of $\chi_{i,s}$ which is about half of that yielded by GYRO and indicated in box 1 of Fig. 3. Under our experimental conditions, the stiffness yielded by the GYRO non-linear simulations seems somewhat too high. The time-averaged profile of T_i is too low in the center. It should be underlined that the GYRO calculations are valid at mid-radius and the transport modeling made with constant coefficients which is very rough and might be improved in the future. Taking for $P_{i,coll}$ the 20% higher PION value increases somewhat T_i and amplitude which tends to improve the match.

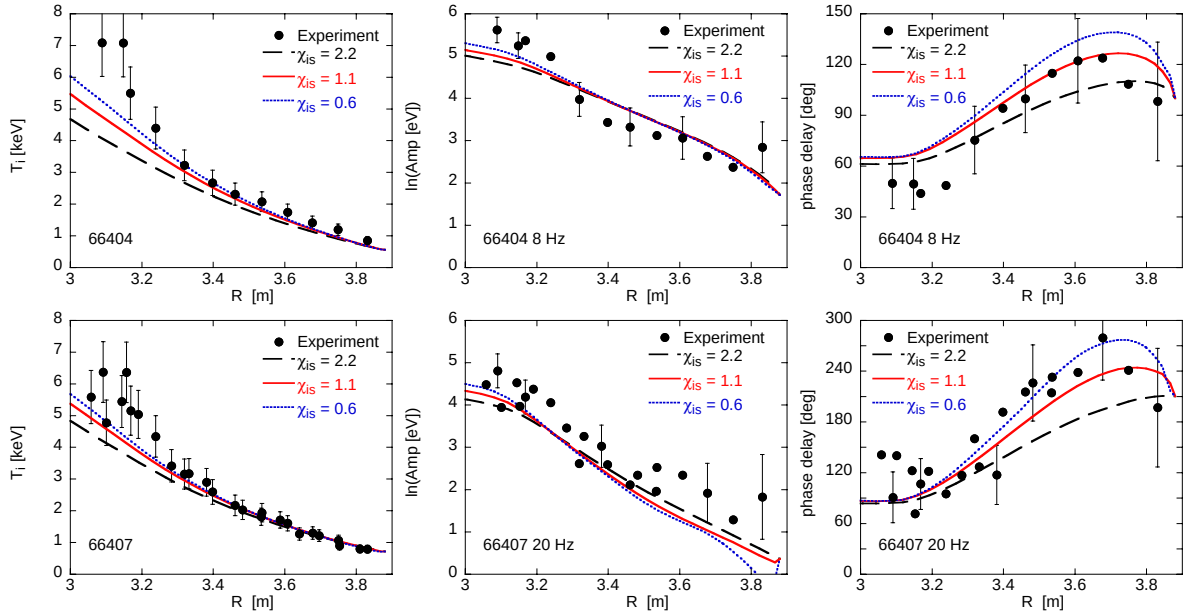

Figure 4: *Time-averaged T_i, amplitude and phase of T_i modulation at 8 (top) and 20 Hz (bottom). Note the different Y-scales of the phase in agreement with the steeper slope at 20Hz.*

The modulation of the electron temperature is more complex and the results presented here are meant as a discussion and should not be considered as definitive so far. The modulation is excited by two heat sources, $P_{e,coll}$ and $P_{e,direct}$, with different profiles and time constants. In addition, as indicated by the gyro-kinetic calculations, the off-diagonal term induced by R/L_{T_i} should also be included. The values derived from GYRO, $\chi_{e,s} \approx 0.05$ and $\chi_{e-i,s} \approx 1.89$, are obtained with very different values of α and cannot be compared directly. The simulations made with these values do not fit the electron experimental data at all. However, it is clear that a strong ITG contribution to electron heat transport must be included, as indicated by Fig. 3. Therefore, taking this knowledge into account, we searched for values of $\chi_{e,s}$ and $\chi_{e-i,s}$ yielding acceptable results. In this search, we set $\alpha = 1$ to simplify, also allowing comparisons between the two contributions and with previous work on electron heat transport. Under these conditions, we obtained acceptable results for the following four cases:
Case a: $\chi_{e,s} = 0.14$, $\chi_{e-i,s} = 0.25$, SELFO powers.
Case b: $\chi_{e,s} = 0.14$, $\chi_{e-i,s} = 0.25$, PION powers.
Case c: $\chi_{e,s} = 0.14$, $\chi_{e-i,s} = 0.25$, SELFO for collisional heating but the larger PION power for $P_{e,direct}$.
Case d: $\chi_{e,s} = 0.35$, $\chi_{e-i,s} = 0$, SELFO powers.

The experimental profiles of T_e, amplitude and phase of the modulation at 8Hz and 20Hz are shown in Fig. 5, together with modeling using the same coefficients for both frequencies. The procedure consisted in adjusting $\chi_{e,s}$ and $\chi_{e-i,s}$ such that the T_e profiles match the experiment, as shown on the left plots. We first focus on the 8Hz case. The middle box indicates that the experimental amplitude does not exhibit any particular feature, except an increase toward the edge which is attributed to a spurious modulation of density excited at the very edge by the RF power and which also reduces the phase there. The modulation amplitude is well reproduced by case c (SELFO with more central direct heating) and very poorly by case b for which the PION $P_{e,coll}$ is clearly to low. Indeed, this agrees with the fact that the collision processes are expected to be better taken into account in SELFO than in PION. The experimental phase exhibits an unusual non-monotonic behaviour at about $R = 3.5$m, which can only be caused by a source-like term with small phase delay. It cannot be caused by fast ^{3}He ions because their phase delay is by far too large. This phase behaviour can be tentatively explained by the three main elements contributing to electron heat transport, $P_{e,direct}$, $P_{e,coll}$ and $\chi_{e-i,s}$, as follows. The centrally deposited heating power $P_{e,direct}$ excites, without phase delay, heat pulses which propagate outwards. At $R \approx 3.2$m, $P_{e,coll}$ induces a second T_e modulation with the significant phase delay indicated above.

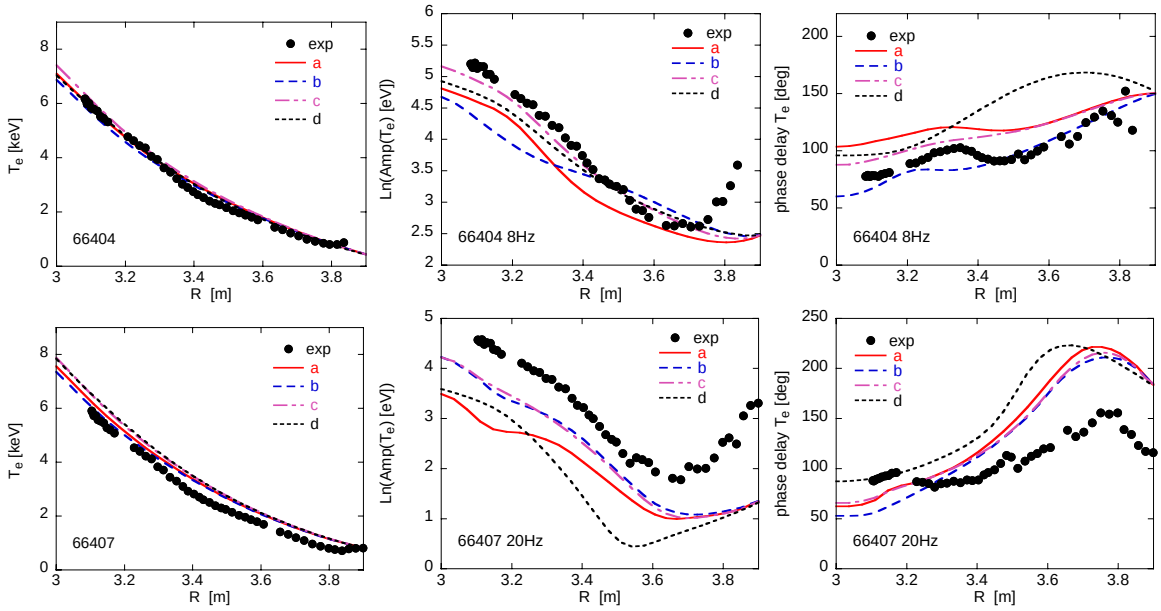

Figure 5: *Time-averaged T_e, amplitude and phase of the T_e modulation at 8 and 20 Hz.*

A third contribution to the T_e modulation is caused by the ion modulation through $\chi_{e-i,s}$, inducing a modulation of T_e related to that of R/L_{T_i}. The modulation amplitude of R/L_{T_i} is zero in the plasma center, exhibits a maximum just outside of the maximum of $P_{i,coll}$ ($R \approx 3.3$ m) and decreases towards the edge. The amplitude profile of the T_e modulation induced by $\chi_{e-i,s}$ has a similar shape but it is, per nature, out of phase with respect to that of R/L_{T_i}. Therefore, it is roughly out of phase with that of the T_e modulation excited by the two electron heat sources and can efficiently reduce the phase delay in the off-axis region. These three components contribute to the measured T_e modulation and can explain the shape of the phase at 8 Hz. We now turn to the 20Hz case. The T_e profile is well also reproduced using the same coefficients as for the 8 Hz case. The experimental amplitude and phase profiles exhibit a usual shape. The absence of the non-monotonic behaviour in the phase is attributed to the fact that the contribution of $P_{e,coll}$ strongly decreases at higher frequency, as well as the effect of $\chi_{e-i,s}$ on the modulation. However, the simulations do not reproduce the modulation data correctly. Whereas, as suggested by case c, the amplitude could be better reproduced by further increasing $P_{e,direct}$, the slope of the phase is not matched at all. A better match would require higher transport leading to a strong mismatch of the T_e profile and this discrepancy is still under investigation.
Alternatively to the existence of the off-diagonal term $\chi_{e-i,s}$, the non-monotonic phase profile at 8Hz and the flat one at 20 Hz could be caused by power deposited off-axis with a small phase delay, therefore not induced by fast ions. Indeed, it is possible to simulate the phase correctly adding an arbitrary electron heating profile with zero phase delay, of different magnitude at 8 and 20 Hz though. In fact, off-axis electron heating due to mode conversion cannot be excluded, [25]. However, the TORIC code, [26], indicates that its radial position is not enough off-axis and its deposition width too narrow, to reproduce the data correctly.

Conclusion

The main goal of the experiment which consisted in investigating ion heat transport with power modulation, has been achieved. The validity of the T_i modulation for transport studies has been demonstrated, yielding for the first time a direct experimental measurement of the ion stiffness. The value found in the present work is moderate which is attributed to the presence of ^{3}He and to the situation $R/L_{T_e} > R/L_{T_i}$, as indicated by the non-linear gyrokinetic results, which agree with the experiment within a factor of 2. The ^{3}He ICRH scheme in deuterium works well for ion modulation and is, to our knowledge, the best possibility for such experiments, despite the accompanying electron heating.
The situation in the electron channel is complex because it involves two heating sources with different

time scales and a significant contribution from the off-diagonal term driven by R/L_{T_i}. Our study indicates that the electron stiffness, $\chi_{e,s} \approx 0.15$, is weak and that the cross term $\chi_{e-i,s} \approx 0.25$ is important. This is due to the ITG-dominated regime and can be different under other experimental situations. The comparison of the ICRF deposition calculated by PION and SELFO for the scheme used here suggests that the fraction of direct electron heating yielded by SELFO might be too low whereas the collisional electron heating from PION is too low and clearly better accounted for by SELFO. An additional off-axis component to electron heating cannot be excluded but it is not identified yet.

Acknowledgment
This work, supported by the European Communities under the contract of Association EURATOM-IPP, was carried out within the framework of the EFDA. The views and opinions expressed herein do not necessarily reflect those of the European Commission.

References
[1] GREENWALD, M. et al., Nucl. Fusion **37** (1997) 793.
[2] SUTTROP, W. et al., Plasma Phys. Controlled Fusion **39** (1997) 2051.
[3] GOHIL, P. et al., Nucl. Fusion **38** (1998) 425.
[4] HORTON, L. D. et al., Plasma Phys. Controlled Fusion **41** (1999) B329.
[5] RYTER, F. et al., Plasma Phys. Controlled Fusion **43** (2001) A323.
[6] URANO, H. et al., Nucl. Fusion **42** (2002) 76 .
[7] PEETERS, A. G. et al., Nucl. Fusion **42** (2002) 1376.
[8]TARDINI, G. et al., Nucl. Fusion **42** (2002) 258.
[9] RYTER, F. et al., Plasma Phys. Controlled Fusion **48** (2006) B453.
[10] RYTER, F. et al., Nucl. Fusion **43** (2003) 1396.
[11] RYTER, F. et al., Phys. Rev. Lett. **95** (2005) 085001.
[12] DEBOO, J. C. et al., Nucl. Fusion **45** (2005) 494.
[13] CAMENEN, Y. et al., Plasma Phys. Controlled Fusion **47** (2005) 1971.
[14] MANTICA, P. et al., Paper EX/2-4, this conference (2008).
[15] TUBBING, B. J. D. et al., Nucl. Fusion **27** (1987) 1843.
[16] LOPES CARDOZO, N. J., Plasma Phys. Controlled Fusion **37** (1995) 799.
[17] MANTICA, P. et al., Comptes Rendus Physique **7** (2006) 634.
[18] CASATI, A. et al., Physics of Plasmas **14** (2007) 092303.
[19] ERIKSSON, L.-G. et al., Nuclear Fusion **33** (1993) 1037.
[20] IMBEAUX, F. et al., Plasma Phys. Controlled Fusion **43** (2001) 1503.
[21] GARBET, X. et al., Plasma Phys. Controlled Fusion **46** (2004) 1351, Addendum in Plasma Physics and Controlled Fusion **47**, 6, pp. 957–958 (2005).
[22] CANDY, J. et al., Journal of Computational Physics **186** (2003) 545.
[23] PEREVERZEV, G. V. et al., IPP report 5/98 (2002) .
[24] PANKIN, A. et al., Computer Phys. Comm. **159** (2004) 157.
[25] MANTSINEN, M. et al., Nucl. Fusion **44** (2004) 33.
[26] BRAMBILLA, M., Plasma Phys. Controlled Fusion **41** (1999) 1.